Brownian Motion of Graphene

Onofrio M. Maragó,[†,*] Francesco Bonaccorso,[‡] Rosalba Saija,[§] Giulia Privitera,[‡] Pietro G. Gucciardi,[†] Maria Antonia Iatì,[†] Giuseppe Calogero,[†] Philip H. Jones,[∥] Ferdinando Borghese,[§] Paolo Denti,[§] Valeria Nicolosi,[⊥] and Andrea C. Ferrari[‡,*]

[†]CNR-Istituto per i Processi Chimico-Fisici, I-98158 Messina, Italy, [‡]Department of Engineering, University of Cambridge, Cambridge CB3 0FA, United Kingdom, [§]Dipartimento di Fisica della Materia e Ingegneria Elettronica, Universitá di Messina, Messina, Italy, [∥]Department of Physics and Astronomy, University College London, WC1E 6BT London, United Kingdom, and [⊥]Department of Materials, University of Oxford, Oxford OX1 3PH, United Kingdom

ABSTRACT Brownian motion is a manifestation of the fluctuation—dissipation theorem of statistical mechanics. It regulates systems in physics, biology, chemistry, and finance. We use graphene as prototype material to unravel the consequences of the fluctuation—dissipation theorem in two dimensions, by studying the Brownian motion of optically trapped graphene flakes. These orient orthogonal to the light polarization, due to the optical constants anisotropy. We explain the flake dynamics in the optical trap and measure force and torque constants from the correlation functions of the tracking signals, as well as comparing experiments with a full electromagnetic theory of optical trapping. The understanding of optical trapping of two-dimensional nanostructures gained through our Brownian motion analysis paves the way to light-controlled manipulation and all-optical sorting of biological membranes and anisotropic macromolecules.

KEYWORDS: Brownian motion · optical tweezers · graphene · electromagnetic scattering theory

The random motion of microscopic particles suspended in a fluid was first observed in the late eighteenth century and goes by the name of Brownian motion (BM).[1] This was ascribed to thermal agitation from the surrounding molecules,[2] leading to Einstein's predictions of the resulting particle displacements.[3] BM is ubiquitous throughout physical, chemical, and biological sciences and even finance. Such random fluctuations can be harnessed to produce directed motion.[4] It was also suggested that thermally activated BM may be responsible for the movement of molecular motors, such as myosin and kinesin.[5]

When a Brownian particle (BP), *i.e.*, a particle undergoing BM in a fluid, is subjected to an external field, *i.e.*, a confining potential, a special class of solutions to the dynamics of its motion occurs, originally studied by Ornstein and Uhlenbeck.[6] The fluid damps the BP motion, and in a high damping regime, such as that of a BP in water, the confining potential acts as a cutoff to the BM dynamics. This is free for short times (high frequency limit), while it is frozen at longer times (low frequency limit).[6] These Ornstein—Uhlenbeck processes have perfect ground in experiments with optical traps, where a BP is held by a focused laser beam, *i.e.*, an optical tweezer.[7] In this context, BM can be utilized to investigate the properties of the surrounding environment,[8,9] as well as of the trapped particle, and for accurate calibration of the spring constants of the optical harmonic potential.[10,11]

Dimensionality plays a special role in nature. From phase transitions,[12] to transport phenomena,[13] two-dimensional (2d) systems often exhibit a strikingly different behavior from those with higher or lower dimensionality.[12] Nanomaterials are an attractive target for optical trapping.[14—16] This can lead to top-down organization of composite nanoassemblies,[14] subwavelength imaging by the excitation and scanning of nano-optical probes,[15] and photonic force microscopy with increased space and force resolution.[16] Graphene[17] is the prototype 2d material and, as such, has unique mechanical, thermal, electronic, and optical properties, already proven outstanding for both fundamental research and applications.[18,19]

Here we demonstrate optical trapping of individual graphene flakes in a water dispersion. This enables the investigation of the anisotropic BP dynamics[20,21] in the optical trap and direct measurement of force and torque constants. The results are understood by a full electromagnetic theory of optical trapping for planar nanostructures.

RESULTS AND DISCUSSION

Graphene is dispersed by processing graphite in a water—surfactant solution, Figure 1a. We do not use any functionalization nor oxidation, in order to retain the electronic structure of pristine graphene in

*Address correspondence to marago@me.cnr.it; acf26@hermes.cam.ac.uk.

Received for review July 28, 2010 and accepted November 03, 2010.

Published online December 2, 2010. 10.1021/nn1018126

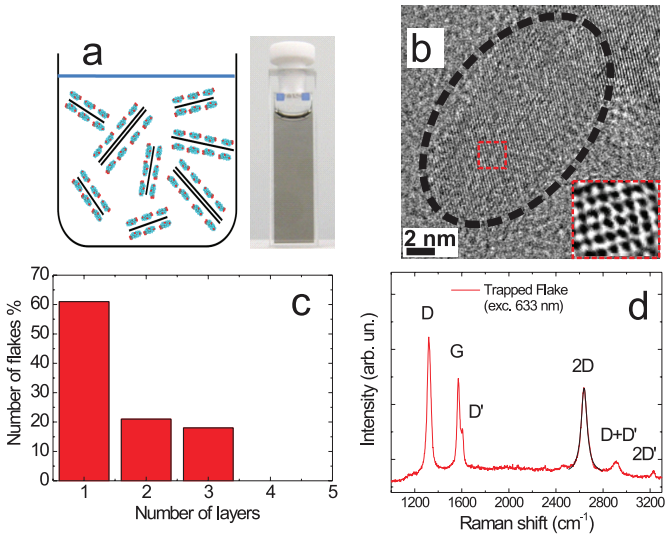

Figure 1. (a) Schematic of water dispersion of graphene and photograph of a dispersion stabilized by SDC. (b) HRTEM image of a representative flake showing the typical graphene honeycomb structure. (c) Histogram of the number of layers per flake obtained from TEM images, showing up to 60% single layer graphene. (d) Raman spectrum of an optically trapped flake for 633 nm trapping and excitation wavelength.

the exfoliated monolayers.[22−24,19,25,26] We use dihydroxy sodium deoxycholate (SDC) as surfactant[27] (see Methods for details).

High resolution transmission electron microscopy (HRTEM) shows flakes with a typical transverse size of tens of nanometer (10−40 nm). Figure 1b is a HRTEM image of one such flake, where the typical graphene honeycomb structure is clearly seen. By analyzing over 100 flakes, we find ∼60% single-layer, with the remainder bi- and trilayers (Figure 1c). This is much higher than previous aqueous[23] and nonaqueous dispersions.[22]

We then place 75 μL of dispersion in a chamber attached to a piezo-stage with 1 nm resolution. Optical trapping is obtained by focusing a near-infrared (NIR; 830 nm) or a helium−neon (633 nm) laser through a 100× oil immersion objective (NA = 1.3) in an inverted configuration (see Methods). The latter is coupled to a spectrometer through an edge filter. This allows us to use the same laser light both for optical trapping and for Raman scattering, realizing a Raman optical tweezer (ROT) to directly probe the structure of the trapped flake, Figure 1d. In both setups, the particles are imaged through the same objective (Figure 2a) that focuses the trapping light onto a charge coupled device (CCD) camera with diffraction limited resolution. Figure 2b shows a free-floating flake, then drawn into the optical trap when the laser is switched on, Figure 2c. When the laser is switched off (Figure 2d) the flake is released and diffuses from the trap region (see the movie in Supporting Information). The minimum power to achieve trapping is ∼1−2 mW .

A typical Raman spectrum of trapped flakes measured at 633 nm is plotted in Figure 1d. Besides the G and 2D peaks, this has significant D and D′ intensities, and the combination mode D + D′ ∼ 2950 cm^{-1}. The G peak corresponds to the E_{2g} phonon at the Brillouin zone center. The D peak is due to the breathing modes of sp^2 rings and requires a defect for its activation by double resonance (DR).[28−30] The 2D peak is the second order of the D peak. This is a single band in monolayer graphene, whereas it splits in four in bilayer graphene, reflecting the evolution of the band structure.[28] The 2D peak is always seen, even when no D peak is present, because no defects are required for the activation of two phonons with the same momentum, one backscattering from the other. DR can also happen intravalley, *i.e.*, connecting two points belonging to the same cone around **K** or **K**′. This gives rise to the D′ peak. The 2D′ is the second order of the D′ peak. The large intensity of the D peak in Figure 1d is not due to the presence of a large amount of structural defects, otherwise it would be much broader, and G and D′ would merge.[29] We rather assign it to the edges of our submicrometer flakes.[31] We note that the 2D band, although broader than in pristine graphene,[28] is still fitted by a Lorentzian. Thus, even if the flakes are multilayers, they are electronically almost decoupled.[32] From the *I*(D)/*I*(G) ratio, we can estimate an order of magnitude for the flakes sizes,[29,30,33] consistent with the HRTEM images.

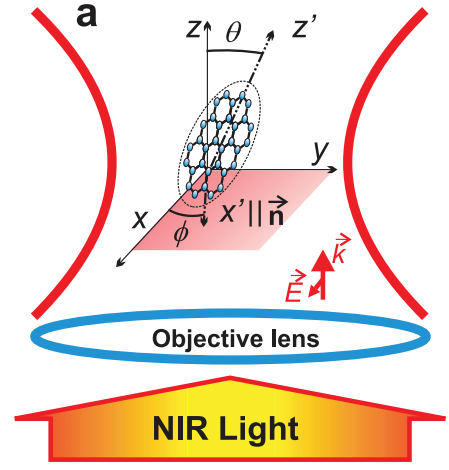

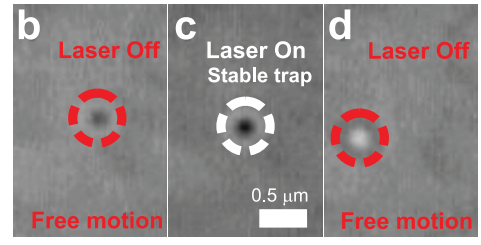

Figure 2. (a) Experimental setup. A laser beam is expanded to overfill the back aperture of a high numerical aperture objective lens. Geometry, relevant angles and axes are also shown. (b) Free floating graphene flake. (c) Laser is switched on and the flake is drawn into the optical trap. (d) Laser is switched off and the flake is released

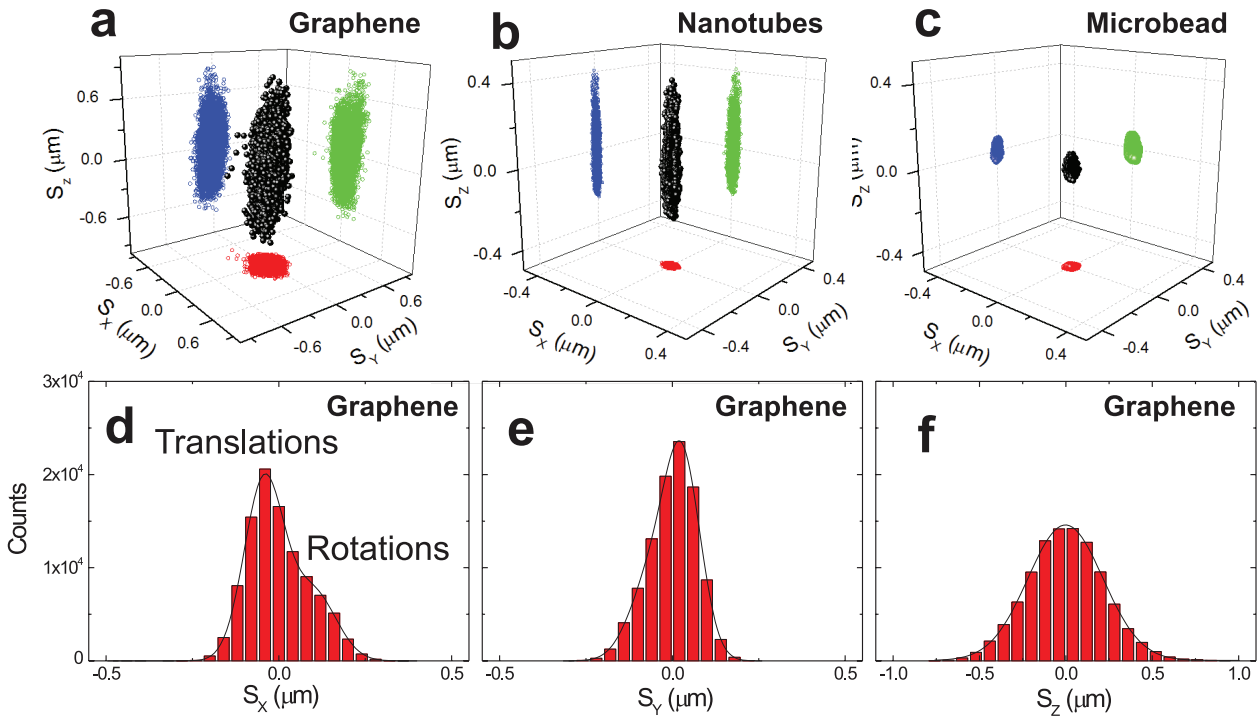

Figure 3. (a) Three-dimensional BM of a flake as compared to that of (b) a nanotube bundle and (c) a latex microbead. 10^4 data points are extracted from the $S_i(t)$ signals acquired for 2 s at 50 kHz sampling rate. (d,e) Histograms of the transverse signals $S_x(t)$,$S_y(t)$. In the transverse direction, both translational and angular fluctuations are superposed. The difference in the root-mean-square widths of the fluctuations in *x* and *y* arises from the graphene flake shape, optical anisotropy, and different curvatures of the optical potential in the directions parallel and perpendicular to the initial polarization. For each graph the QPD voltage-to-position calibration factors β_i are obtained using the calculated mobility coefficients and amplitude of the signals' autocorrelation functions $C_{ii}(0) = \beta_i^2 k_B T/k_i$ for the position fluctuation contributions only. The root mean squares of the transverse displacements, extracted from a Gaussian fit, are $\sqrt{\langle x^2 \rangle} = 57 \pm 2$ nm and $\sqrt{\langle y^2 \rangle} = 53 \pm 2$ nm. While for rotations we obtain $\sqrt{\langle \phi^2 \rangle} = 0.11 \pm 0.01$ rad (about 7 deg), consistent with the small angle approximation. (f) Histogram of the longitudinal signal $S_z(t)$. This is only due to center of mass fluctuations and root-mean-square of $\sqrt{\langle z^2 \rangle} = 217 \pm 5$ nm.

The flakes positional and angular displacements in the optical trap are detected by back focal plane (BFP) interferometry using the forward scattered light from the trapped particle.[10,16] The BFP interference pattern is determined by the flake orientation through the relevant angles (ϕ,θ), see Figure 2a. Because the trapped flake is aligned with the *yz* plane, fluctuations occur in the small angle limit, $\phi \ll 1$,$\theta \ll 1$, and the particle tracking signals in the Cartesian directions are (see Methods)

$$S_x \sim \beta_x(X - a\phi + b\theta); S_y \sim \beta_y(Y + c\phi); S_z \sim \beta_z Z \quad (1)$$

where β_i are the detector calibration factors, *X*, *Y*, and *Z* are the center-of-mass coordinates, and a, b, c are constants that are dependent on flake geometry and optical constants. S_z is not much affected by angular motion, having a cos θ dependence only.

Figure 3a visualizes the three-dimensional BM of a flake, reconstructed from the tracking signals, compared with that of a nanotube bundle (Figure 3b) and a spherical latex microbead (Figure 3c), measured in the same apparatus, under the same experimental conditions. It is clear that these 2d, 1d, and 3d objects exhibit distinct behaviors. The difference in the dynamics is due to the particle shape and optical properties. For a spherical particle, the hydrodynamics is isotropic.[9,10] Therefore, the different extent of fluctuations from equilibrium is only due to the anisotropy of the optical potential.[11,34] For a linear nanostructure, anisotropic hydrodynamics leads to a much increased mobility along the optical axis.[16] In contrast, our flake has increased fluctuations in both longitudinal and transverse directions, which we ascribe to a higher contribution from rotational motion with respect to nanotubes. As discussed later, this is a fingerprint of the 2d geometry, yielding an increased sensitivity to angular fluctuations about the optical axis. The large optical anisotropy of graphene enhances this further, aligning the flake orthogonal to the light polarization. The effect of the rotational BM is illustrated in the histograms of Figure 3d−f, where the contribution from a superposition of translational and rotational fluctuations is seen in the transverse directions, but is absent in the longitudinal.

To extract quantitative data, we first analyze the flake hydrodynamics, which encompasses translational and rotational motions. The viscous drag and torque are described by the anisotropic mobility tensors[20,21] Γ^t_{ij} for translations, and Γ^r_{ij} for rotations (see Supporting Information). These are related to the fluid dynamical viscosity η (0.911 mPa s for water at 24 °C) and particle size. We approximate the flakes as extremely flat ellip-

soids, with transverse size Δ much larger than their height h, consistent with the overall thickness of the SDC covered flake, $h \sim 1$ nm, giving $h/\Delta \approx 0.04 \ll 1$. This allows us to exploit the analytic solutions for uniaxial ellipsoids of Perrin[20] (see Supporting Information). The hydrodynamic mobilities are then only a function of η and Δ:

$$\Gamma_{\parallel} \approx \frac{1}{8\eta\Delta} \quad \Gamma_{\perp} \approx \frac{3}{16\eta\Delta} \quad \Gamma^{r} \approx \frac{3}{4\eta\Delta^{3}} \tag{2}$$

In this approximation, the rotational mobility has the same value for any axis through the center-of-mass, while the parallel translation mobility is 2/3 the perpendicular one. From HRTEM, we have $\Delta \sim 25$ nm. Thus, $\Gamma_{\parallel} \sim 5.49$ μm /(fN s), $\Gamma_{\perp} \sim 8.26$ μm /(fN s), and $\Gamma^{r} \sim 52.6$ (fN nm s) $^{-1}$. Within this framework we describe the Brownian dynamics of trapped graphene by a set of uncoupled Langevin equations:[12]

$$\partial_t X_i(t) = -\omega_i X_i(t) + \xi_i(t), \; i = x, y, z \tag{3}$$

$$\partial_t \phi(t) = -\Omega_\phi \phi(t) + \xi_\phi(t) \tag{4}$$

$$\partial_t \theta(t) = -\Omega_\theta \theta(t) + \xi_\theta(t) \tag{5}$$

where X_i, ϕ, and θ are stochastic variables associated with the position and angular coordinates, $\xi_i(t)$ are random noise sources with zero mean and variance $\langle \xi_i(t)\xi_i(t+\tau)\rangle = 2k_B T \Gamma_i \delta(\tau)$, while $\omega_i = \Gamma_i k_i$, $\Omega_\phi = \Gamma^r k_\phi$, and $\Omega_\theta = \Gamma^r k_\theta$ are relaxation frequencies related to the force and torque constants and mobility tensor components. The torque of the confining potential on the lab axes is only relevant for orientational dynamics, while not affecting center-of-mass motion in a small angle regime. Also, due to the strong *yz* alignment and because angular fluctuations are small, the radiation torque along *y* (affecting θ) is small and $\Omega_\theta \approx 0$.

We now evaluate the temporal correlations between the particle tracking signals, equation (1), which yield the trap parameters.[16,35] For a nonspherical particle, correlation function analysis reveals information about center-of-mass and angular fluctuations, hence on trap force and torque constants.[16] For the strongly aligned 2d graphene flake, the autocorrelation of the transverse tracking signal $C_{ii}(\tau) = \langle S_i(t)S_i(t+\tau)\rangle$ decays with lag time τ as a double exponential corresponding to positional and angular relaxation frequencies ω_i ($i = x, y$), Ω_ϕ, whereas, because the stochastic variables are uncorrelated in the small angle regime, the cross-correlations $C_{xy}(\tau) = \langle S_x(t)S_y(t+\tau)\rangle$ of the transverse signals decay as a single exponential with a relaxation rate corresponding to Ω_ϕ (see Supporting Information).

These allow us to derive the optical force constants from the relaxation frequency measurements, as follows. Figure 4a is a representative autocorrelation function analysis of the transverse tracking signals $C_{ii}(\tau) = \langle S_i(t)S_i(t+\tau)\rangle$ ($i = x,y$). These data are well fitted by two exponentials with $\omega_x = (8.6 \pm 0.2) \times 10^3$ s^{-1}, $\omega_y = (12.9 \pm 0.3) \times 10^3$ s^{-1} for the translational decay rates and $\Omega_\phi = (3.0 \pm 0.1) \times 10^2$ s $^{-1}$ for the angular fluctuations decay rate (obtained as the averaged value from the C_{xx} and C_{yy} slow relaxation rate). Figure 4B shows that the autocorrelation of the axial signal C_{zz} is well fitted by a single exponential decay with rate $\omega_z = (7.70 \pm 0.05) \times 10^2$ s^{-1}. In Figure 4C the cross-correlation of the transverse signals C_{xy} is shown (for positive lag time only) fitted by a single exponential with decay rate $\Omega_\phi = (2.90 \pm 0.05) \times 10^2$ s^{-1}, consistent with the value obtained from the autocorrelation functions. Repeating these measurements over ten different flakes, and using our estimation of the hydrodynamic mobility parameters calculated above (Figure 3), we obtain the spring constants $k_i = \omega_i/\Gamma_i$ to be $k_x = 1.1 \pm 0.4$ pN/μm, $k_y = 1.3 \pm 0.5$ pN/μm, $k_z = 0.08 \pm 0.03$ pN/μm and torque constant about the propagation direction $k_\phi = \Omega_\phi/\Gamma^r = 9 \pm 3$ fmN · nm/rad, where the uncertainty takes into account the 40% spread on flake size. Note how the measured force constants only depend on the flake transverse size, and not on thickness, because of the 2d geometry that strongly effects both the hydrodynamics and the radiation force and torque.

We calculate the radiation force and torque using the full scattering theory in the transition matrix (T-matrix) framework.[34,36] We first consider the incident field configuration in the focal region of a high NA lens in absence of any particle.[34] The radiation force $\mathbf{F}_{rad}$ and torque $\mathbf{G}_{rad}$ are calculated considering linear and angular momentum conservation for the combined system of field and graphene[36] (see Supporting Information). The dielectric constant of graphene is a highly anisotropic tensor[37−42] with components $\varepsilon_\perp$ and $\varepsilon_\parallel$ in the directions perpendicular and parallel to the *c* axis (see Figure 2a for the geometry with relevant axes and angles).[40] For $\lambda = 830$ nm, the graphene refractive index is $n_\perp = 3 + i1.5$ and $n_\parallel = 1.694$.[40,42] Note that the imaginary part of the perpendicular refractive index yields a large absorption, while the parallel imaginary part is negligible. We then calculate $\mathbf{F}_{rad}(\mathbf{r})$, the argument $\mathbf{r}$ denoting the center of mass of graphene relative to the focal point (see Figure 2a). Trapping occurs when the radiation force vanishes with a negative derivative, Figure 4g. Due to the symmetry of both graphene and electromagnetic field in the focal region,[34] trapping occurs on the optical axis. For small displacements from equilibrium, the single-beam optical trap is well approximated by an harmonic potential $V(x_i) = 1/2\sum_{i=x,y,z} k_i x_i^2$ with spring constants $k_z < k_x$ and k_y. These depend on both the geometry of the trapped particle and the parameters of the propagating focused Gaussian beam, such as power and polarization.[16,34]

The flake orientation is specified by the angles ϑ,φ, Figure 2a. For each orientation, we first determine the

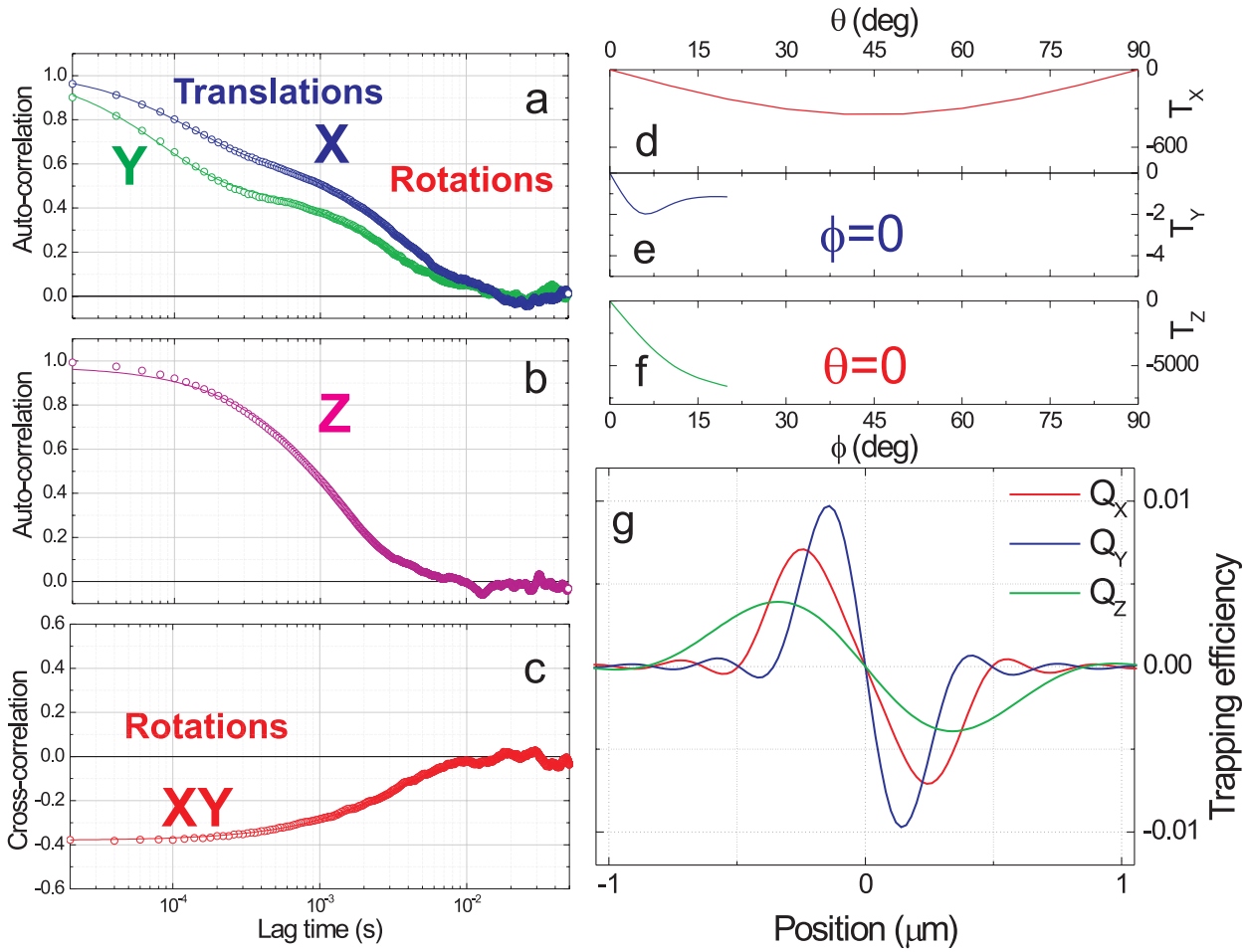

Figure 4. (a) Transverse (*x*,*y*) and (b) longitudinal (*z*) signal autocorrelation functions. A double exponential decay is seen in the transverse autocorrelations, arising from the different time scales of translational and angular BM with $\omega_x = (8.6 \pm 0.2) \times 10^3\ s^{-1}$, $\omega_y = (12.9 \pm 0.3) \times 10^3\ s^{-1}$ for the translational decay rates and $\Omega_\phi = (3.0 \pm 0.1) \times 10^2\ s^{-1}$ for the angular one. While a single exponential decay is observed in the axial (*z*) direction with $\omega_z = (7.70 \pm 0.05) \times 10^2\ s^{-1}$. Solid lines are exponential fits to the data. (c) Transverse signal cross-correlation function revealing only angular fluctuations. The decay rate is consistent with that of the slower part of the transverse autocorrelation. The negative sign is related to the 2d graphene geometry, resulting in an opposite phase in *x* and *y*, during rotation. (d−f) Calculated optical torque components. A stable orientation is obtained when the flake lies in the *yz*-plane (orthogonal to the polarization axis). For T_y and T_z, no data is shown for ϕ, $\theta > 20°$ because the flake is expelled from the trap by radiation pressure above this critical value. The polarization torque (T_z) is 2 orders of magnitude higher than the other components. (g) The optical trapping efficiency components $Q_i = cF_{rad,i}/nP$ (*c* velocity of light, $n = 1.33$ water refractive index, and *P* laser power) are proportional to the optical force, for a flake in the equilibrium orientation. For small displacements from equilibrium the force follows Hooke's law and the derivatives at the equilibrium position define the force constants k_x, k_y, and k_z.

trapping position of the center of mass and then calculate the torque relative to each axis at that position (Figure 4d−f):

$$\mathbf{T} = \frac{8\pi k}{n^2 |E_0|^2 \sigma_T} \mathbf{G}_{rad} \qquad (6)$$

where E_0 is the amplitude of the incident field, σ_T is the flake extinction cross section, and $n = 1.33$ the water refractive index. The orientational stability occurs when **T** vanishes with a negative derivative with respect to both θ and ϕ (Figure 4d−f). We find that stable trapping is achieved when the flake plane is parallel to *yz*. When the polarization axis lies on the flake plane (*e.g.*, when the flake is parallel to *xy* or *xz*), the radiation pressure is so strong that the flake is pushed out of the trap. This is a consequence of the large imaginary part of $\varepsilon_\perp$. As shown in Figure 4d−f the flake is stable under small angle rotations around its equilibrium orientation, while for larger values of ϕ and θ (>20°) it is expelled from the trap by radiation pressure. Moreover, the polarization torque (T_z) is a hundred times larger than the other components because of the anisotropy of the optical constants.

Note that flat microparticles with pronounced shape anisotropy, but no optical anisotropy, were shown to orient in an optical trap with their basal plane parallel to the incident polarization axis.[43] In the case of graphene, a significant difference in trapping behavior occurs, resulting in an orientation orthogonal to the incident polarization axis. This is related to the strong optical anisotropy of graphene, resulting in an orientation dependent radiation pressure. Thus, there is an

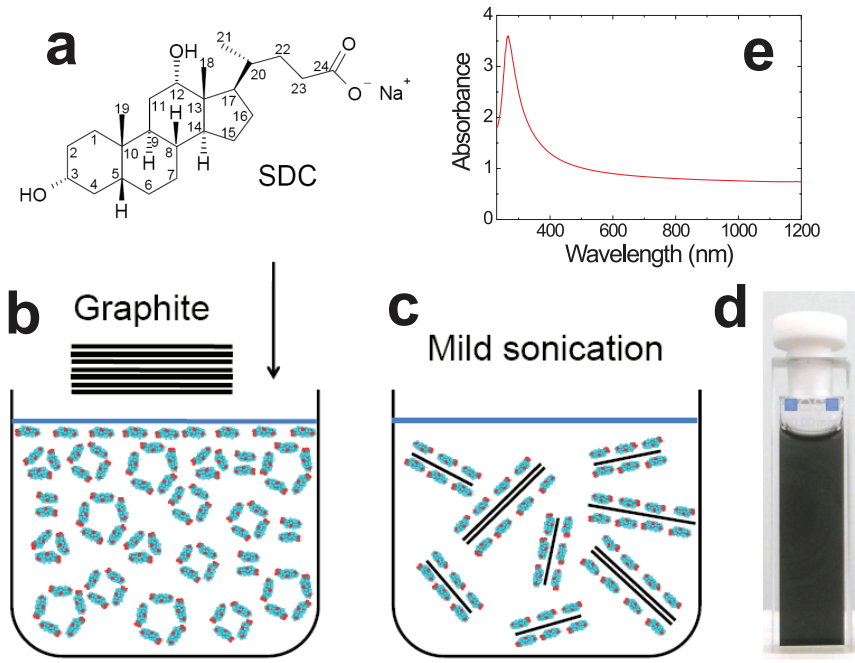

Figure 5. Graphite exfoliation. (a) Molecular structure of SDC. (b) Schematic illustration of the graphite exfoliation process. (c) A mild ultrasonication exfoliates mono- and few-layer graphene encapsulated by SDC. (d) Photograph of the dispersion before ultracentrifugation. (e) Absorption measurement for the resulting dispersion.

interplay between optical and shape anisotropy, crucial in determining the diffusion of graphene in the optical trap. Understanding this is of crucial importance when light forces are used to hold, manipulate, or assemble nanostructures.[14−16]

CONCLUSIONS

We optically trapped and spectroscopically resolved individual graphene flakes, revealing their angular fluctuations and elucidating their anisotropic dynamics and hydrodynamics. The center-of-mass and angular contributions to the tracking signals were separated by a correlation function analysis, and both optical force and torque constants measured. We calculated the radiation force and torque from a full electromagnetic scattering theory showing that graphene orientation in the optical trap is driven by light polarization. The graphene dimensionality and consequent strong anisotropy in both optical and hydrodynamic properties determine the flake stability in optical trapping. The ability to discriminate linear and angular motion is of great importance for the fundamental understanding of the optical trapping mechanisms of planar structures. Our results and methodology are generic and can be extended to any type of 2d nanostructures, such as biological membranes. Our investigation of trapped graphene demonstrates that the optical trap provides an ideal environment for spectroscopic and mechanical probing of such structures, linking their Brownian Motion dynamics to their form and interactions.

METHODS

Graphite Exfoliation. Graphene dispersions are prepared from the exfoliation of kish graphite (Sigma-Aldrich). 0.2 mg/mL are added to 10 mL deionized (DI) water with 0.3% w/v sodium deoxycholate (SDC, Sigma Aldrich) dihydroxy bile salt. The organic anion of SDC is a cholesterol derivative of amphiphilic nature with about 60% of its water-exposed surface hydrophobic, and the rest hydrophilic (Figure 5a).[44] These amphiphilic molecules, with a hydrophobic and a hydrophilic side,[27] disperse graphene in aqueous solution by physical adsorption on its surface. In contrast to linear chain surfactants, *i.e*, sodium dodecylbenzene sulfonate (SDBS), widely used for SWNTs,[45−48] the flat structure of SDC disperses graphene more efficiently. We selected SDC, among all dihydroxy and trihydroxy bile salts, due to its highest hydrophobic index,[26] *i.e.*, the ratio between the hydrophobic and hydrophilic areas.[49] Higher index indicates stronger hydrophobicity, fundamental in the interaction (adsorption) of flat molecules in aqueous solution.[49] The hydrophobic SDC patches bind graphene *via* hydrophobic interactions. At the same time, the SDC polar groups hydrophilicity makes the graphene−surfactant complex dispersible in water.[26]

Graphite is first added to the SDC aqueous solution, Figure 5b. The resultant dispersion is heated at 90 °C for 2 h and then mild ultrasonicated for 90 min in a bath sonicator. During ultrasonication, the strong hydrodynamic shear-force, created by the propagation of cavitons,[50,51] induces exfoliation. The SDC molecules β side attaches to the dispersed flakes. The ensuing steric hindrance prevents their re-aggregation, Figure 5c,d. A sedimentation based-separation in a centrifugal field is then used to separate the flakes by size and shape. The dispersion is ultracentrifuged at 5k RPM (~1280 g) at 15 °C in a fixed angle rotor MLA-80 (Beckman- Coulter Optima Max-E) for 30 min. The optical properties of the flakes are not significantly affected by the surfactant molecules at our trapping wavelengths (830 and 633 nm), as shown by the optical absorption spectra in Figure 5e. In particular, we note the flat absorption in the near-infrared spectral region, consistent with that previously measured in free-standing graphene and graphene on a substrate.[37−39]

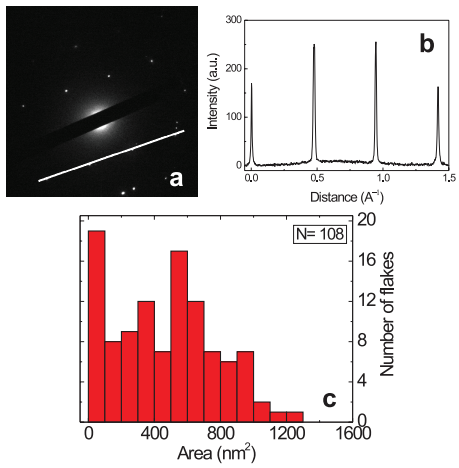

Figure 6. TEM analysis. (a) Electron diffraction pattern of a flake image. (b) Intensity analysis of the diffraction pattern along the dotted line shown in (a). First order peaks have a higher intensity than second order ones, as expected for a monolayer.[22,23] (c) Histogram of the flakes surface area.

For TEM measurements (Figure 6) the dispersion is drop cast onto holey carbon grids (400 mesh). Images are taken with a JEOL JEM2200MCO FEGTEM/STEM, with two CEOS Cs aberration correctors, at 80 kV.

Optical Trapping Setup. Our optical tweezers set-ups are sketched in Figure 7a,b. They both have an inverted configuration (*i.e.*, the light propagates upward) and are equipped with an Olympus Uplan FLN × 100 NA 1.3 objective, which tightly focuses a near-infrared (NIR) and red laser beam for optical trapping, imaging, and Raman scattering.

The NIR laser tweezers (Figure 7a) is equipped with a 830 nm diode laser. Its beam is circularized using an anamorphic prism pair. The power is ~16 mW over a spot size ~0.64 μm. Particle motion in the NIR tweezers is detected by means of back focal plane (BFP) interferometry,[10] whereby the interference pattern between forward scattered and unscattered light in the back aperture of the microscope condenser is imaged onto a four-quadrant photodiode (QPD). The outputs from all quadrants are processed as pairwise and four-quadrant sums in order to have signals proportional to the trapped particle displacement in the three directions (particle tracking signals).[10] From these signals we derive the optical trap spring constants in all three dimensions (hence, a calibration of optical trapping forces against hydrodynamic forces) and, more generally, information on positional and orientational Brownian dynamics.[16,35,52]

The integration of Raman spectroscopy is obtained in the red, Figure 7b. The beam of a HeNe laser (Melles Griot 05-LHP-991, 633 nm, $P = 9$ mW) is expanded by a telescope (magnification 4:1), overfilling the objective, then reflected by an aluminum mirror toward an edge filter (Semrock LP02-633RU-25, band-pass 641−1427.4 nm, transition width <150 cm^{-1}). The incidence angle is 5°. The laser beam is therefore reflected toward the microscope objective focusing on a diffraction limited spot (~0.49 μm diameter). The graphene dispersion is contained in a liquid chamber mounted on a piezostage (Physics Instruments, P-517.3CL) allowing for 100 × 100 × 20 μm^3 movement in *xyz* with 1 nm resolution. The backscattered light passes through the edge filter, used for Rayleigh scattering removal, and is subsequently focused by a 50 mm lens onto a Jobin-Yvon Triax 190 spectrometer (190 mm focal length) equipped with a 1200 L/mm grating blazed at 650 nm. An avalanche photodiode (Perkin-Elmer SPCM-AQRH-16, dark counts <25 cts/sec, photon detection efficiency 65% at 650 nm) is used for light detection. A beam splitter can be inserted in the optical path to reflect 50% of the light toward a CCD camera (Thorlabs USB 2.0, DCU223M) allowing for visual inspection of the trapped particle. Raman spectra are typically acquired with integration times of 0.1−1 s. Setting the monochromator slits to 100 μm yields a resolution of 15 cm^{-1} guaranteeing good S/N ratio even for 100 ms integration.

In optical trapping experiments, heating effects are typically due to light absorption in the solvent,[53] rather than in trapped

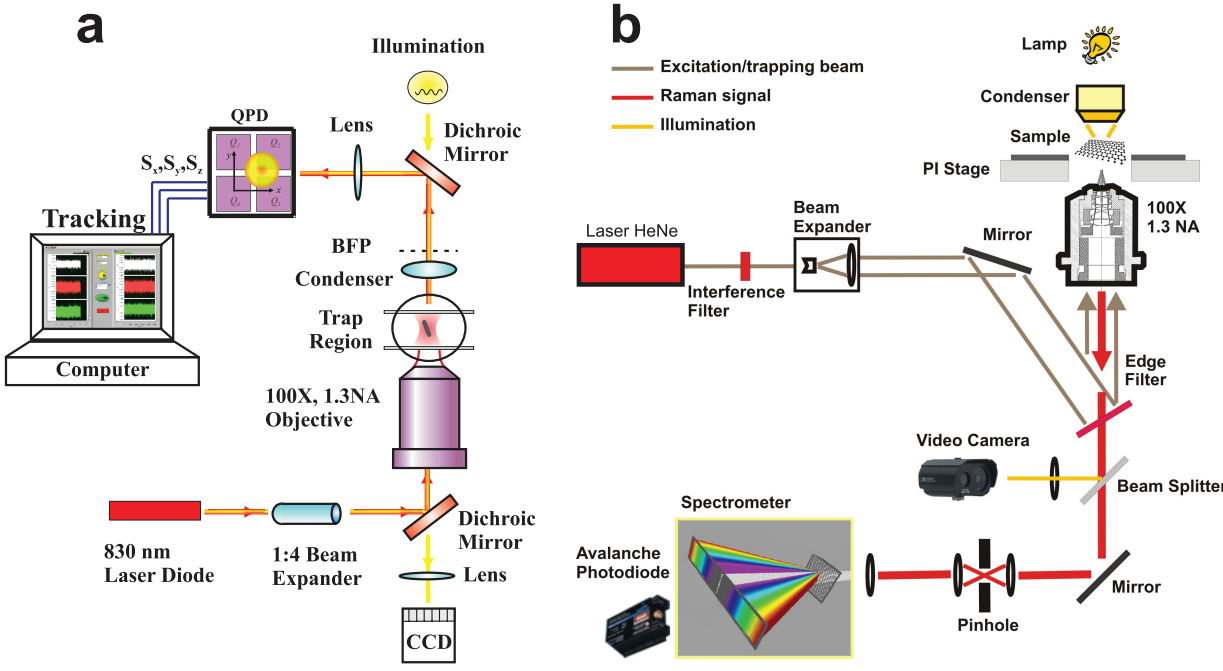

Figure 7. (a) NIR optical tweezers. The light from a laser diode at 830 nm is expanded and sent through a 1.3 NA objective. Samples are loaded in a small chamber where the focused light traps individual graphene flakes. The forward scattered and unscattered light is collected by a condenser lens and sent to a quadrant photodiode for tracking. The same optics is used to image the sample with a lamp on a CCD camera. (b) Raman tweezers. Light at 633 nm from a He−Ne laser is used to both trap and perform Raman scattering. The laser is tightly focused through an oil immersion objective into a chamber containing the graphene dispersion. The backscattered light is collected by the same 1.3 NA objective, dispersed through a grating spectrometer and detected with a single photon avalanche photodiode. An edge filter is used to both reflect the laser light and cut the Rayleigh scattering from the back-reflected radiation.

particles. We can estimate the absorption on the trapped particles as[54]

$$P_{abs} = 2\pi n^2 \frac{I_0}{\lambda} \mathrm{Im}\left(\frac{\alpha}{\varepsilon_0}\right) \quad (7)$$

where $n = 1.33$ is the water refractive index, I_0 is the field intensity, λ is the trapping wavelength, α is the graphene polarizability, and Im denotes the imaginary part. This can be expressed in terms of the real ε_1 and imaginary ε_2 dielectric constants through the Clausius-Mossotti relation:[54]

$$\mathrm{Im}\left(\frac{\alpha}{\varepsilon_0}\right) = V \frac{\varepsilon_2 n^2}{(\varepsilon_1 + 2n^2)^2 + \varepsilon_2^2} \quad (8)$$

Because of graphene optical anisotropy, we need to consider the different contribution to the absorption from the different polarization directions in the focal region. A laser beam with an incident *x*-polarization has components with off-axis polarization in the focus.[54] The *y*-polarization component is negligible, while the *z* component has an intensity ~10% of the total. Graphene orients with its basal plane orthogonal to the *x*-polarization axis. Thus, $P_{abs} \sim 0.9P_{\parallel} + 0.1P_{\perp}$, where $P_{\parallel}$ and $P_{\perp}$ are the absorbed powers calculated with out-of-plane and in-plane dielectric constants, $\varepsilon_{\parallel}$ and $\varepsilon_{\perp}$. Because is, $\varepsilon_{\parallel,2}$ is 10^{-4},[40,55] $\varepsilon_{\perp,2} = 2.25$,[40] $\varepsilon_{\parallel,1} = 2.87$,[40] and $\varepsilon_{\perp,1} = 9$,[40] this yields $P_{abs} \sim 0.2$ pW, $P_{\perp} \sim 1.3$ nW. Thus, we can estimate the total power absorbed by trapped flake to be $P_{abs} \sim 0.13$ nW. This is 3 orders of magnitude lower than the power absorbed by the water surrounding the flake within the focal region[53] and confirms that the radiation extinction is dominated by scattering processes. The laser induced heating for the water surrounding the trap region can be estimated from Ref. 53, where the local water heating for near infrared irradiation was measured to be ~7.9K/W. Four our 16mW trapping power, this would give a ~0.13K temperature increase.This is well below any measurable effect. Thus heating is negligible, and the small absorbed power is quickly dissipated in the surrounding environment.

Acknowledgment. We thank E. Lidorikis and O. Trushkevych for useful discussions. We acknowledge funding from EPSRC Grants GR/S97613/01, EP/E500935/1, the ERC Grant NANOPOTS, a Royal Society Brian Mercer Award for Innovation. F.B. acknowledges funding from a Newton International Fellowship. A.C.F. is a Royal Society Wolfson Research Merit Award holder.

Supporting Information Available: Descriptions of optical trapping theory of graphene, hydrodynamics of graphene, Langevin equations, correlation function of the quadrant photodiode signals, and a video showing optical trapping of a flake. This material is available free of charge *via* the Internet at http://pubs.acs.org.

REFERENCES AND NOTES

1. Brown, R. A Brief Account of Microscopical Observations Made on the Particles Contained in the Pollen of Plants. *Philos. Mag.* **1828**, *4*, 161–173.
2. Gouy, L. G. Note Sur Le Mouvement Brownien. *J. Phys. (Paris)* **1888**, *7*, 561–564.
3. Einstein, A. Über Die Von Der Molekularkinetischen Theorie Der Wärme Geforderte Bewegung Von in Ruhenden Flüssigkeiten Suspendierten Teilchen. *Ann. Phys.* **1905**, *17*, 549–560.
4. Jones, P. H.; Goonasekera, M.; Renzoni, F. Rectifying Fluctuations in an Optical Lattice. *Phys. Rev. Lett.* **2004**, *93*, 073904.
5. Astumian, R. D. Thermodynamics and Kinetics of a Brownian Motor. *Science* **1997**, *276*, 917–922.
6. Uhlenbeck, G. E.; Ornstein, L. S. On the Theory of Brownian Motion. *Phys. Rev.* **1930**, *36*, 823–841.
7. Ashkin, A.; Dziedzic, J. M.; Bjorkholm, J. E.; Chu, S. Observation of a Single-Beam Gradient Force Optical Trap for Dielectric Particles. *Opt. Lett.* **1986**, *11*, 288–290.
8. Svoboda, K.; Block, S. M. Biological Applications of Optical Forces. *Annu. Rev. Phys. Biomol. Struct.* **1994**, *23*, 247–285.
9. Martin, S.; Reichert, M.; Stark, H.; Gisler, T. Direct Observation of Hydrodynamic Rotation-Translation Coupling between Two Colloidal Spheres. *Phys. Rev. Lett.* **2006**, *97*, 248301.
10. Pralle, A.; Prummer, M.; Florin, E.-L.; Stelzer, E. H. K.; Hörber, J. K. H. Three-Dimensional High-Resolution Particle Tracking for Optical Tweezers by Forward Scattered Light. *Microsc. Res. Tech.* **1999**, *44*, 378–386.
11. Rohrbach, A. Stiffness of Optical Traps: Quantitative Agreement Between Experiment and Electromagnetic Theory. *Phys. Rev. Lett.* **2005**, *95*, 168102.
12. Le Bellac, M.; Mortessagne, F.; Batrouni, G. G. *Equilibrium and Non-Equilibrium Statistical Thermodynamics*; Cambridge University Press: U.K., 2004.
13. Heinzel, T. *Mesoscopic Electronics in Solid State Nanostructures*, 2nd ed.; Wiley-VCH Verlag: Germany, 2007.
14. Pauzauskie, P. J.; Radenovic, A.; Trepagnier, E.; Shroff, H.; Yang, P.; Liphardt, J. Optical Trapping and Integration of Semiconductor Nanowire Assemblies in Water. *Nat. Mater.* **2006**, *5*, 97–111.
15. Nakayama, Y.; Pauzauskie, P. J.; Radenovic, A.; Onorato, R. M.; Saykally, R. J.; Liphardt, J.; Yang, P. Tunable Nanowire Nonlinear Optical Probe. *Nature* **2007**, *447*, 1098–1102.
16. Maragó, O. M.; Jones, P. H.; Bonaccorso, F.; Scardaci, V.; Gucciardi, P. G.; Rozhin, A.; Ferrari, A. C. Femtonewton Force Sensing with Optically Trapped Nanotubes. *Nano Lett.* **2008**, *8*, 3211–3216.
17. Novoselov, K. S.; Geim, A. K.; Morozov, S. V.; Jiang, D.; Zhang, Y.; Dubonos, S. V.; Grigorieva, I. V.; Firsov, A. A. Electric Field Effect in Atomically Thin Carbon Films. *Science* **2004**, *306*, 666–669.
18. Geim, A. K.; Novoselov, K. S. The Rise of Graphene. *Nat. Mater.* **2007**, *6*, 183–191.
19. Bonaccorso, F.; Sun, Z.; Hasan, T.; Ferrari, A. C. Graphene Photonics and Optoelectronics. *Nat. Photonics* **2010**, *4*, 611–622.
20. Perrin, F. Mouvement Brownien d'un Ellipsoide (I). Dispersion Dielectrique pour des Molecules Ellipsoidales. *J. Phys. Rad.* **1934**, *5*, 497–511.
21. Han, Y.; Alsayed, A. M.; Nobili, M.; Zhang, J.; Lubensky, T. C.; Yodh, A. G. Brownian Motion of an Ellipsoid. *Science* **2006**, *314*, 626–630.
22. Hernandez, Y.; Nicolosi, V.; Lotya, M.; Blighe, F. M.; Sun, Z. Y.; De, S.; McGovern, I. T.; Holland, B.; Byrne, M.; Gun'ko, Y. K.; et al. High-Yield Production of Graphene by Liquid-Phase Exfoliation of Graphite. *Nat. Nanotechnol.* **2008**, *3*, 563–568.
23. Lotya, M.; Hernandez, Y.; King, P. J.; Smith, R. J.; Nicolosi, V.; Karlsson, L. S.; Blighe, F. M.; De, S.; Wang, Z. M.; McGovern, I. T.; et al. Liquid Phase Production of Graphene by Exfoliation of Graphite in Surfactant/Water Solutions. *J. Am. Chem. Soc.* **2009**, *131*, 3611–3620.
24. Sun, Z.; Hasan, T.; Torrisi, F.; Popa, D.; Privitera, G.; Wang, F.; Bonaccorso, F.; Basko, D. M.; Ferrari, A. C. Graphene Mode-Locked Ultrafast Laser. *ACS Nano* **2010**, *4*, 803–810.
25. Blake, P.; Brimicombe, P. D.; Nair, R. R.; Booth, T. J.; Jiang, D.; Schedin, F.; Ponomarenko, L. A.; Morozov, S. V.; Gleeson, H. F.; Hill, E. W.; et al. Graphene-Based Liquid Crystal Device. *Nano Lett.* **2008**, *8*, 1704–1708.
26. Hasan, T; Torrisi, F.; Sun, Z.; Popa, D.; Nicolosi, V.; Privitera, G.; Bonaccorso, F.; Ferrari, A. C. Solution-Phase Exfoliation of Graphite for Ultrafast Photonics. *Phys. Status Solidi B* **2010**, 1–5 (DOI: 10.1002/pssb.201000339).
27. Roda, A.; Hofmann, A. F.; Mysels, K. J. The Influence of Bile Salt Structure on Self-association in Aqueous Solutions. *J. Biol. Chem.* **1983**, *258*, 6362–6370.
28. Ferrari, A. C.; Meyer, J. C.; Scardaci, V.; Casiraghi, C.; Lazzeri, M.; Mauri, F.; Piscanec, S.; Jiang, D.; Novoselov, K. S.; Roth, S.; et al. Raman Spectrum of Graphene and Graphene Layers. *Phys. Rev. Lett.* **2007**, *97*, 187401.
29. Ferrari, A. C.; Robertson, J. Interpretation of Raman Spectra of Disordered and Amorphous Carbon. *Phys. Rev. B* **2000**, *61*, 14095–14107.

30. Tuinstra, F.; Koenig, J. Raman Spectrum of Graphite. *J. Chem. Phys.* **1970**, *53*, 1126–1130.
31. Casiraghi, C.; Hartschuh, A.; Qian, H.; Piscanec, S.; Georgi, C.; Fasoli, A.; Novoselov, K. S.; Basko, D. M.; Ferrari, A. C. Raman Spectroscopy of Graphene Edges. *Nano Lett.* **2009**, *9*, 1433–1441.
32. Latil, S.; Meunier, V.; Henrard, L. Massless Fermions in Multilayer Graphitic Systems with Misoriented Layers: Ab Initio Calculations and Experimental Fingerprints. *Phys. Rev. B* **2007**, *76*, 201402(R).
33. Cancado, L. G.; Takai, K.; Enoki, T.; Endo, M.; Kim, Y. A.; Mizusaki, H.; Jorio, A.; Coelho, L. N.; Magalhaes-Paniago, R.; Pimenta, M. A. General Equation for the Determination of the Crystallite Size L_a of Nanographite by Raman Spectroscopy. *Appl. Phys. Lett.* **2006**, *88*, 163106.
34. Borghese, F.; Denti, P.; Saija, R.; Iatí, M. A. Optical Trapping of Nonspherical Particles in the T-Matrix Formalism. *Opt. Express* **2007**, *15*, 11984–11998.
35. Jones, P. H.; Palmisano, F.; Bonaccorso, F.; Gucciardi, P. G.; Calogero, G.; Ferrari, A. C.; Maragó, O. M. Rotation Detection in Light-Driven Nanorotors. *ACS Nano* **2009**, *3*, 3077–3084.
36. Borghese, F.; Denti, P.; Saija, R.; Iatí, M. A.; Maragó, O. M. Radiation Force and Torque on Optically Trapped Linear Nanostructures. *Phys. Rev. Lett.* **2008**, *100*, 163903.
37. Casiraghi, C.; Hartschuh, A.; Lidorikis, E.; Qian, H.; Harutyunyan, H.; Gokus, T.; Novoselov, K. S.; Ferrari, A. C. Rayleigh Imaging of Graphene and Graphene Layers. *Nano Lett.* **2007**, *7*, 2711–2717.
38. Nair, R. R.; Blake, P.; Grigorenko, A. N.; Novoselov, K. S.; Booth, T. J.; Stauber, T.; Peres, N. M. R.; Geim, A. K. Fine Structure Constant Defines Visual Transparency of Graphene. *Science* **2008**, *320*, 1308.
39. Mak, K. F.; Sfeir, M. Y.; Wu, Y.; Lui, C. H.; Misewich, J. A.; Heinz, T. F. Measurement of the Optical Conductivity of Graphene. *Phys. Rev. Lett.* **2008**, *101*, 196405.
40. Kravets, V. G.; Grigorenko, A. N.; Nair, R. R.; Blake, P.; Anissimova, S.; Novoselov, K. S.; Geim, A. K. Spectroscopic Ellipsometry of Graphene and an Exciton-shifted van Hove Peak in Absorption. *Phys. Rev. B* **2010**, *81*, 155413.
41. Lidorikis, E.; Ferrari, A. C. Photonics with Multiwall Carbon Nanotube Arrays. *ACS Nano* **2009**, *3*, 1238–1248.
42. Schedin, F.; Lidorikis, E.; Lombardo, A.; Kravets, V. G.; Geim, A. K.; Grigorenko, A. N.; Novoselov, K. S.; Ferrari, A. C. Surface-Enhanced Raman Spectroscopy of Graphene. *ACS Nano* **2010**, *4*, 5617–5626.
43. Galajda, P.; Ormos, P. Orientation of Flat Particles in Optical Tweezers by Linearly Polarized Light. *Opt. Express* **2003**, *11*, 446–451.
44. Small, D. M.; Penkett, S. A.; Chapman, D. Studies on Simple and Mixed Bile Salt Micelles by Nuclear Magnetic Resonance Spectroscopy. *Biochim. Biophys. Acta* **1969**, *176*, 178–189.
45. Islam, M. F.; Rojas, E.; Bergey, D. M.; Johnson, A. T.; Yodh, A. G. High Weight Fraction Surfactant Solubilization of Single-Wall Carbon Nanotubes in Water. *Nano Lett.* **2003**, *3*, 269–273.
46. Moore, V. C.; Strano, M. S.; Haroz, E. H.; Hauge, R. H.; Smalley, R. E. Individually Suspended Single-Walled Nanotubes in Various Surfactants. *Nano Lett.* **2003**, *3*, 1379–1382.
47. Scardaci, V.; Rozhin, A. G.; Hennrich, F.; Milne, W. I.; Ferrari, A. C. Carbon Nanotubes—Polymer Composites for Photonic Devices. *Phys. E* **2007**, *37*, 115–118.
48. Bonaccorso, F.; Hasan, T.; Tan, P. H.; Sciascia, C.; Privitera, G.; Di Marco, G.; Gucciardi, P. G.; Ferrari, A. C. Density Gradient Ultracentrifugation of Nanotubes: Interplay of Bundling and Surfactants Encapsulation. *J. Phys. Chem C* **2010**, *114*, 17267–17285.
49. Miyajima, K.; Machida, K.; Taga, T.; Komatsu, H.; Nakagaki, M. Correlation between the Hydrophobic Nature of Monosaccharides and Cholates, and their Hydrophobic Indices. *J. Chem. Soc., Faraday Trans. 1* **1988**, *84*, 2537–2544.
50. Masselin, I.; Chasseray, X.; Durand-bourlier, L.; Laineb, J.-M.; Syzaretc, P.-Y.; Lemordantet, D. Effect of Sonication on Polymeric Membranes. *J. Membr. Sci.* **2001**, *181*, 213–220.
51. Mason, T. J. *Sonochemistry*; Oxford University Press: New York, 1999.
52. Volpe, G.; Petrov, D. Torque Detection using Brownian Fluctuations. *Phys. Rev. Lett.* **2006**, *97*, 210603.
53. Peterman, E. J. G.; Gittes, F.; Schmidt, C. F. Laser-Induced Heating in Optical Traps. *Biophys. J.* **2003**, *84*, 1308–1316.
54. Novotny, L.; Hecht, B. *Principles of Nano-Optics*; Cambridge University Press: U.K., 2006.
55. Djurisic, A. B.; Li, E. H. Optical Properties of Graphite. *J. Appl. Phys.* **1999**, *85*, 7404–7410.